Engineering 17 (2022) 75–81

Contents lists available at ScienceDirect

Engineering

journal homepage: www.elsevier.com/locate/eng

Research
Metamaterials—Article

Super-Resolution Displacement Spectroscopic Sensing over a Surface "Rainbow" †

Lyu Zhou [a,#], Nan Zhang [a,#], Chang Chieh Hsu [b], Matthew Singer [a], Xie Zeng [a], Yizheng Li [a], Haomin Song [a], Josep Jornet [c], Yun Wu [b], Qiaoqiang Gan [a,d,*]

[a] Department of Electrical Engineering, The State University of New York at Buffalo, Buffalo, NY 14260, USA
[b] Department of Biomedical Engineering, The State University of New York at Buffalo, Buffalo, NY 14260, USA
[c] Department of Electrical and Computer Engineering, Northeastern University, Boston, MA 02115, USA
[d] Material Science Engineering Program, King Abdullah University of Science and Technology, Thuwal 23955-6900, Saudi Arabia

ARTICLE INFO

Article history:
Received 5 October 2021
Revised 3 February 2022
Accepted 1 March 2022
Available online 8 July 2022

Keywords:
Rainbow trapping
Metasurface
Surface plasmon polaritons
Super-resolution displacement
On-chip biosensing

ABSTRACT

Subwavelength manipulation of light waves with high precision can enable new and exciting applications in spectroscopy, sensing, and medical imaging. For these applications, miniaturized spectrometers are desirable to enable the on-chip analysis of spectral information. In particular, for imaging-based spectroscopic sensing mechanisms, the key challenge is to determine the spatial-shift information accurately (i.e., the spatial displacement introduced by wavelength shift or biological or chemical surface binding), which is similar to the challenge presented by super-resolution imaging. Here, we report a unique "rainbow" trapping metasurface for on-chip spectrometers and sensors. Combined with super-resolution image processing, the low-setting 4× optical microscope system resolves a displacement of the resonant position within 35 nm on the plasmonic rainbow trapping metasurface with a tiny area as small as 0.002 mm^2. This unique feature of the spatial manipulation of efficiently coupled rainbow plasmonic resonances reveals a new platform for miniaturized on-chip spectroscopic analysis with a spectral resolution of 0.032 nm in wavelength shift. Using this low-setting 4× microscope imaging system, we demonstrate a biosensing resolution of 1.92×10^9 exosomes per milliliter for A549-derived exosomes and distinguish between patient samples and healthy controls using exosomal epidermal growth factor receptor (EGFR) expression values, thereby demonstrating a new on-chip sensing system for personalized accurate bio/chemical sensing applications.

1. Introduction

Imaging-based sensing technologies are major tools for visualizing essential biological or chemical information. However, due to the classic optical diffraction limit, conventional optical imaging systems are usually bulky and expensive to enable better imaging capabilities. Ultra-slow waves on the nanoscale are of great interest due to their unique potential for improved light–matter interactions in miniaturized nanoplasmonic structures [1–4]. In particular, the trapped "rainbow" storage of light in metamaterials [5] and plasmonic graded structures [6–9] has opened up new and attractive approaches to manipulate light on a chip. Recent investigations of various photonic nanostructures [1–14] have demonstrated that surface dispersion properties can be tuned by systematically varying the geometric parameters of the surface gratings (e.g., groove depth and grating period [6–9]). The dispersion relations for adiabatically graded gratings vary monotonically with position, so incoming waves at different wavelengths can be "trapped" or localized at different positions along the propagation direction of the grating.

It is believed that this type of on-chip wavelength-splitting functionality will result in miniaturized spectrometer platforms (e.g., Refs. [15–17]) for future optical integration [8,9,17–21]. More recently, a similar wavelength-splitting functionality was implemented in several graded plasmonic grating structures [22–24] and all-dielectric metasurfaces [25,26], realizing an exciting

† The data that support the findings of and the custom codes used in this study are available from the corresponding author, Q. Gan, upon reasonable request.

* Corresponding author.
E-mail address: qiaoqiang.gan@kaust.edu.sa (Q. Gan).
# These authors contributed equally to this work.

https://doi.org/10.1016/j.eng.2022.03.018

on-chip imaging-based sensing system [25–29]. For these imaging-based, intensity-modulation, and/or wavelength-modulation sensing mechanisms, the key challenge is to determine the spatial information accurately [30–32], which is similar to the challenge presented by super-resolution imaging [33]; that is, there is a need for the capability to detect nanometric displacement in spatial position or wavelength domain. This is the key to realizing ultra-sensitive on-chip imaging and sensing technologies.

2. Design principles

Here, we demonstrate a plasmonic "rainbow" trapping metasurface to achieve super-resolution identification of the spatial pattern shift due to plasmonic resonances that can be realized using low-setting optical microscope imaging systems. As illustrated in Fig. 1(a), a shallow metallic surface grating with graded geometric parameters is fabricated on an opaque metal film (270 nm thick; see the next section for fabrication details). Depending on the local geometries, different incident wavelengths of a broadband incident light can be efficiently coupled to the surface plasmon polaritons (SPPs) on the graded metasurface, resulting in an on-chip rainbow distribution of resonances.

Fig. 1(b) shows a scanning electron microscope (SEM) image of a graded surface grating with the overall dimensions of 30 μm × 64 μm. According to the atomic force microscope (AFM) characterization, the average depth of the surface grating is 35.6 nm ± 0.4 nm (see Fig. S1 in Appendix A for characterization results). The period of the gratings varies from 250 to 850 nm, with a step size of about 5 nm (see Fig. S2 in Appendix A for SEM characterization). Under white light illumination, we recorded the grating's reflection images, demonstrating a clear rainbow color, as shown in Fig. 1(c) (see Section S3 and Fig. S3 in Appendix A for optical measurement details). This spatial wavelength splitting introduced by the rainbow trapping effect [20] is sensitive to local dielectric environment perturbation, enabling spatial displacement imaging and sensing on a chip. To analyze the rainbow trapping mechanism, four narrowband wavelengths (i.e., 500, 530, 590, and 650 nm) were introduced by a liquid-crystal tunable filter to illuminate the sample. Their corresponding grey-scale top-view images are shown in Fig. 1(d) (upper panels of images at each wavelength). A dark bar was clearly observed at different locations due to the efficient coupling of SPP modes.

To reveal the physics of this graded metasurface, a two-dimensional (2D) finite-difference time domain (FDTD) simulation was performed to plot the near-field distribution of the launched SPP modes, clearly showing the rainbow coupling along the graded surface grating. As shown in the lower panels in Fig. 1(d), the side view of the 2D electric field distribution demonstrates that the SPPs can be launched and localized at different regions on the graded metasurface (i.e., for a trapped rainbow [8]; see simulation details in Section S4 in Appendix A). As a result, a dark region appears in the far-field reflection image of the surface grating, which agrees well with the experimental observation. Intriguingly, the reflection dip in the far field (i.e., the top dark red arrow in Fig. 1(d)) corresponds to the localized SPP modes on the graded grating surface (i.e., the bottom red arrow in Fig. 1(d)). When the incident wavelength or surface refractive index is changed, both the near-field and far-field features change accordingly (see Section S4). The most sensitive sensing region lies within the trapped SPP modes region on the graded metasurface, which is slightly different from the far-field scattering dark region due to the unique

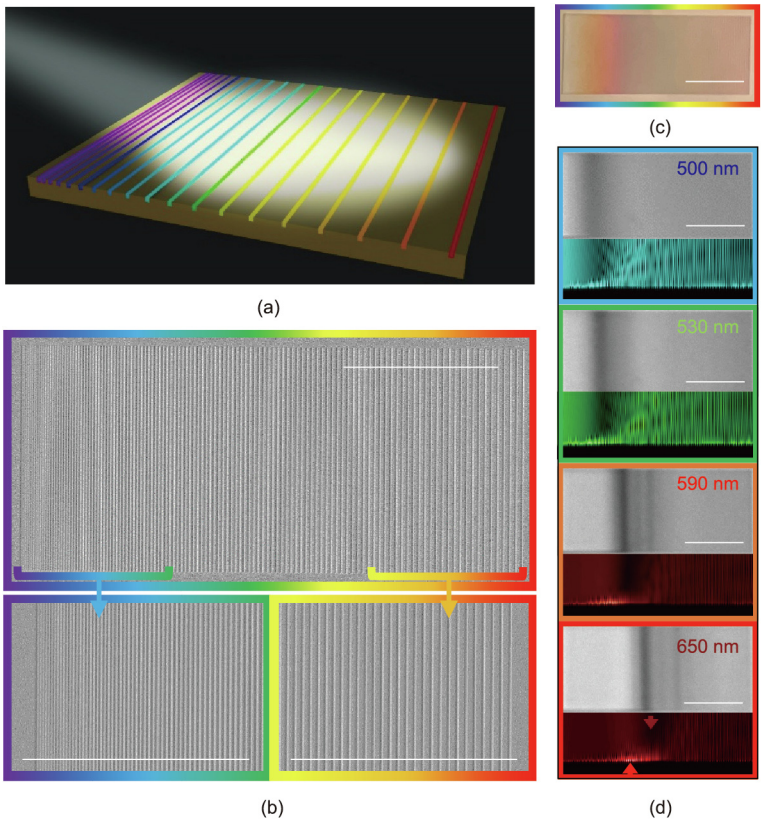

Fig. 1. Graded "rainbow" trapping metasurface. (a) Schematic diagram of a "rainbow" trapping metasurface. (b) SEM images of a graded grating with the overall dimensions of 30 μm × 64 μm. Bottom insets show differences in periodicity from the left edge of the sample to the right edge (scale bar: 20 μm). (c) Reflection image of the graded grating under white light illumination (observed by a 4× microscope; scale bar: 20 μm). (d) Monochromatic top-view reflection images (upper panels) and their corresponding simulated side-view electric field distributions in near field (lower panels) at different incident wavelengths (scale bar: 20 μm).

coupling and scattering feature of the rainbow trapping metasurface (see more details in Section S4 and Fig. S4 in Appendix A). As a result, it is possible to realize new and powerful on-chip spectroscopic analysis and surface sensing by monitoring the spatial shift of the reflection dip in the far field using simple and inexpensive optics.

3. Materials and methods

Fused silica wafers (Semiconductor Wafer, Inc.) were cleaned using acetone, methanol, and deionized (DI) water by immersion in an ultrasonic bath for 10 min at each step, respectively. A 5 nm-thick titanium (Ti) adhesion layer followed by a 270 nm-thick gold (Au) film were deposited on the fused silica wafers using an electron beam evaporator (AXXIS, Kurt J. Lesker Company) at a deposition rate of 0.02 nm•s^{-1}. A AURIGA CrossBeam (Carl Zeiss AG) focused ion beam (FIB)-SEM was used for FIB and SEM characterization. All groove widths were set to 180 nm. Using this fabricated rainbow trapping metasurface, we then developed a super-resolution displacement spectroscopic imager.

4. Results and discussion

4.1. Trapped "rainbow" super-resolution displacement spectroscopic imager

Here, we first demonstrated an on-chip "rainbow" spectroscopic imager by selecting five narrowband wavelengths to illuminate the sample (Fig. 2(a)). Since the SPP modes are dependent on the incident angle of the input light, a collimated incident light is desirable for controlled optical coupling. Therefore, we introduced a 4× objective lens with a small numerical aperture (NA) of 0.13 (corresponding to the largest incident angle of 7.47°) to observe the reflection image. Under this condition, a dark bar was clearly observed due to the efficient coupling of SPP modes (Fig. 2(b)). Intriguingly, as the incident wavelength was tuned from 560 to 680 nm with a step size of 30 nm (Fig. 2(a)), the dark bar shifted accordingly (Fig. 2(b)). Thus, by resolving the spatial position of the dark bar, it is possible to perform on-chip spectroscopic analysis. In this imaging-based apparatus, the optical diffraction gratings and long optical paths used in conventional spectrometers for high spectral resolution are replaced by a rainbow trapping metasurface on the chip that can be directly imaged by charge-coupled device (CCD) or complementary metal oxide semiconductor (CMOS) cameras. Remarkably, the spectral resolution of this on-chip imager spectrometer is well beyond the diffraction limit of the imaging system, as demonstrated below.

In conventional spectroscopic displacement applications (e.g., wavelength modulation for plasmonic biosensing [34–36]), resonant peak or valley positions are fitted to show the trace refractive index change of the sensor surface. Therefore, a higher resolution in wavelength shift identification is desirable in more sensitive spectroscopic analysis and sensing. In the experiment shown in Fig. 2(b), the image was obtained through a 4× microscope. At this magnification, each pixel corresponds to a spatial dimension of approximately 1.6 μm. Therefore, the physical resolution of the low-setting imaging system imposes a technical limit onto this on-chip spectrometer. In particular, the valley positions of these dark bars are unclear due to the relatively broad bandwidth of the grating coupler (Fig. S5 in Appendix A). To address this challenge, we borrow a concept from super-resolution imaging to identify the physical or geometric centroid of the pattern (e.g., the point spread function was used to extract the centroid of fluorescent dye molecules [37–39]). For each wavelength shown in Fig. 2(a), we captured 50 frames (0.2 s per frame) and calculated their centroids (see details in Section S6 in Appendix A). As shown in Fig. 2(c), 50 centroids of each wavelength are localized within a 0.02-pixel

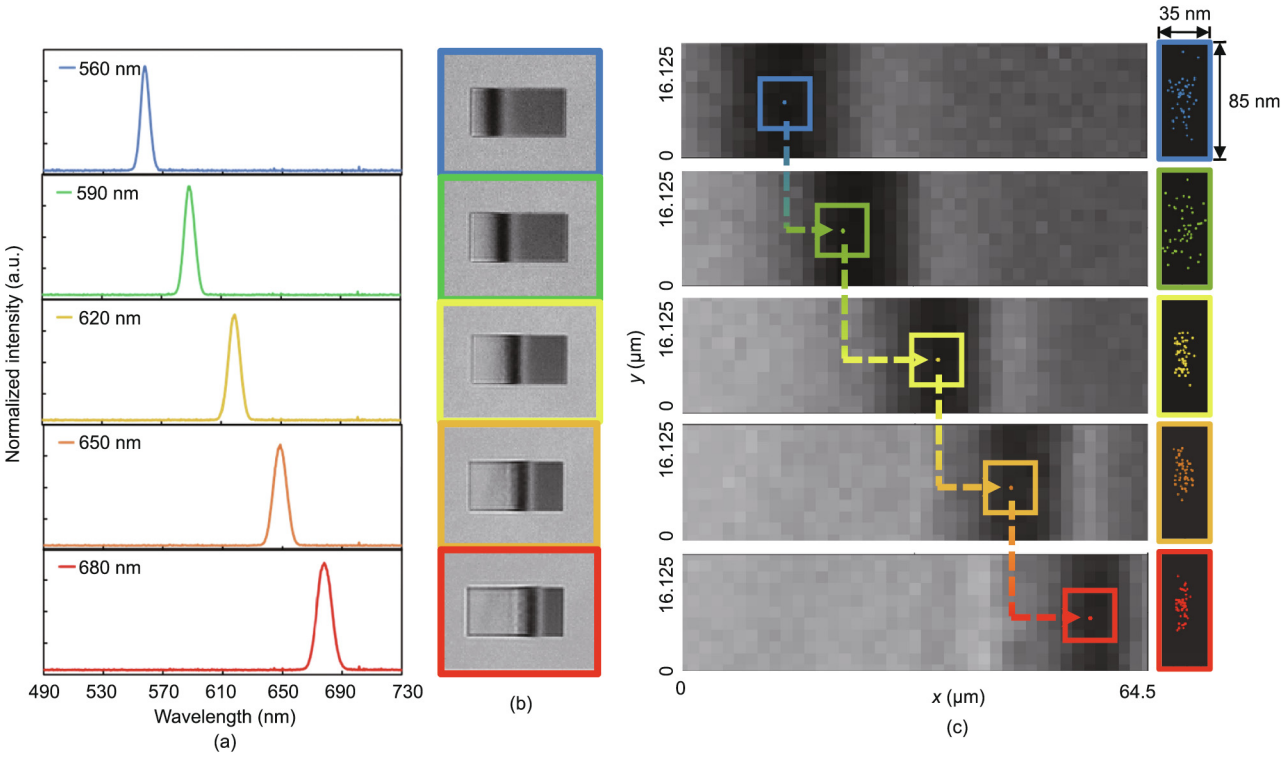

Fig. 2. Trapped "rainbow" localization images for spectral analysis observed by a 4× objective lens. (a) Incident spectra measured by a regular fiber-based spectrometer (a.u.: arbitrary unit). (b) Reflection images under the illumination of five selected wavelengths. (c) Centroid localization of 50 frames at each wavelength. All centroids are localized within 0.02 pixels. Right panels: zoom-in views of 50 centroids observed at each wavelength.

region along the *x*-axis. Remarkably, the standard deviations (SDs) of the five images are all within 35 nm (see the right panel of Fig. 2(c)). Therefore, the wavelength resolution is not limited by the actual pixel size (i.e., ~1.6 μm) or the diffraction limit (λ/(2NA), ranging from 2.04 to 2.50 μm for the incident wavelength tuned from 560 to 680 nm), but by the extracted centroid localization region (i.e., <35 nm × 85 nm), which is well beyond the optical resolution in this 4× optical microscope system. For example, the spatial distance of the two localization positions at the wavelengths of 560 and 590 nm is approximately 8.8 μm (indicated by the dashed line and the arrow in Fig. 2(c)). Considering the SD of the centroid localization at these two wavelengths, the wavelength resolution of this imager can be obtained. Next, we will perform a more finely controlled experiment to reveal the wavelength identification capability of this rainbow localization imaging spectrometer.

In order to reveal the potential of the trapped rainbow for centroid localization, we fabricated a new structure with much smaller period changes (i.e., from 460 to 540 nm with a step size of 1 nm). As shown in Fig. 3(a), we tuned the peak wavelength of the incident light from 548.0 to 549.5 nm with a step size of 0.3 nm. This wavelength shift resolution is close to the limit of the fiber-based spectrometer used in this experiment [40]. Under the illumination of these six finely separated wavelengths, we recorded the dark bars of the graded grating using the 4× objective lens, as shown in the right panel of Fig. 3(a). As shown in these raw images, it is difficult to resolve the spatial shift of the dark bar with the naked eye (detailed images are provided in Fig. S7 in Appendix A). In contrast, the centroid localizations of the dark bars are plotted in Fig. 3(b). Remarkably, these centroid localizations can be clearly separated with no spatial overlap, as shown in the lower panel of Fig. 3(b). As the incident wavelength was tuned from 548.0 to 549.5 nm, the centroid shifted by about 0.74 pixels, with an estimated wavelength-shift resolution of 0.032 nm (see details in Table S1 in Section S8 in Appendix A). The spatial limit of detection (i.e., three times the SD) is about 0.0766 μm—much smaller than the pixel size or diffraction limit of this 4× microscope (~1.61 and ~2.12 μm, respectively)—revealing the super-resolution capability of the rainbow trapping grating structure paired with the centroid data-processing method.

To further reveal the wavelength resolution, we then employed a 20× long working distance objective lens to observe the trapped rainbow. In this case, each pixel corresponds to a dimension of about 0.32 μm. The NA of the lens is 0.25, corresponding to the largest incident angle of approximately 14.48°. Therefore, the dark bar region is slightly different from the one observed by the 4× objective lens due to the different coupling and collection angle, as shown in Fig. 3(c). To tune the dark bar to the center of the sample, we changed the peak wavelength of the incident light from 539.0 to 540.5 nm with a step size of 0.3 nm. The corresponding centroid localizations are plotted in Fig. 3(d), showing that the total displacement is about 0.39 μm when the incident wavelength is tuned by 1.5 nm. Remarkably, the SD of the centroid localization region in this image is better than the 4× imaging system. The wavelength resolution observed under this 20× objective lens is about 0.029 nm (see details in Table S2 in Section S8 in Appendix A). This result indicates that the resolution can be improved with an objective lens of higher magnification.

As a control experiment, we also characterized the centroid localization of the spectra measured by a commercial fiber-based

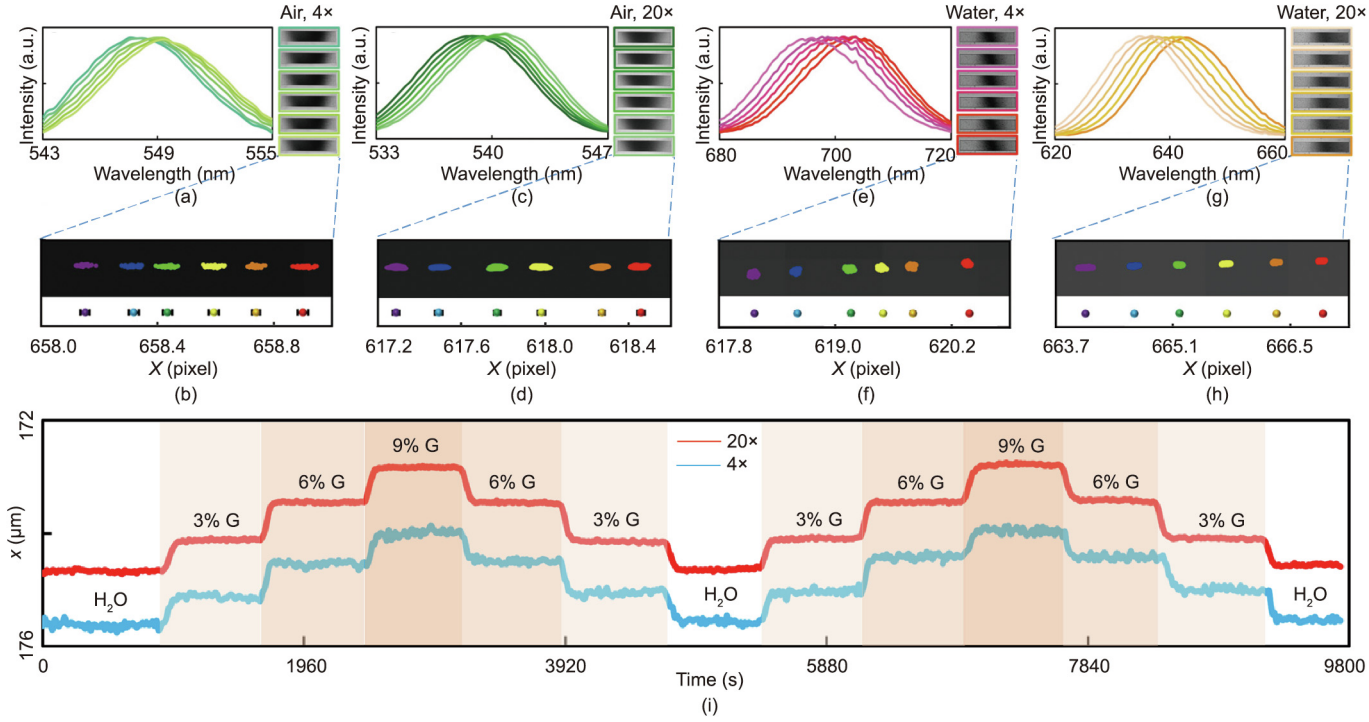

Fig. 3. Spectral displacement resolution of the trapped rainbow localization microscopic spectrometer. (a–d) Observation in air: (a) Left panel is the measured spectra of the incident light with a peak range from 548.0 to 549.5 nm, and right panel is the 4× microscopic reflection images under the illumination of the six incident wavelengths; (b) centroid localization of 50 frames at each wavelength (upper panel) and the average centroid positions with their corresponding SDs (lower panel; see details in Table S1); (c) left panel is the measured spectra of the incident light with a peak range from 539.0 to 540.5 nm, and right panel is the 20× microscopic reflection images; (d) centroid localization at each wavelength (upper panel) and the average centroid positions (lower panel). (e–h) Observation in water: (e) Left panel is the measured spectra of the incident light with a peak range from 696.0 to 701.0 nm, and right panel is the 4× microscopic reflection images; (f) centroid localization (upper panel) and the averaged centroid positions (lower panel); (g) left panel is the measured spectra of the incident light with a peak range from 636.0 to 641.0 nm, and right panel is the 20× microscopic reflection images; (h) centroid localization (upper panel) and average centroid positions (lower panel) at these six incident wavelengths. (i) Real-time centroid movement of the rainbow surface grating pattern under the 4× (blue curve) and 20× (red curve) objective lens in response to different concentrations of glycerol (G)–water solutions.

spectrometer. The SD of the measured spectra was about 0.047 nm (corresponding to a wavelength-shift resolution of ~0.020 nm; see details in Table S5 in Section S9 in Appendix A). Therefore, our rainbow grating structure can realize a similar wavelength shift resolution compared with a commercial spectrometer when centroid-based processing is implemented. Importantly, the distinguishing feature is that the spectral information from a very small area (i.e., the rainbow grating area in the range of 30 μm × 64 μm to 50 μm × 250 μm, i.e., 0.00192–0.01250 mm^2) can be resolved by the imaging-based on-chip spectrometer, indicating the potential of 2D spectroscopic imaging, which is challenging to realize using conventional fiber-based spectrometers.

4.2. Refractive index sensing

To demonstrate how this rainbow trapping chip could be applied for surface biosensing, we fabricated a new graded grating with a period that changes from 400 to 490 nm (observation results are shown in Figs. 3(e)–(h)). As shown by the right panels in Figs. 3(e) and (g), the dark bars were tuned to the center of the structure in the water environment under the illumination of 696–701 nm light (for the 4× objective lens, Fig. 3(e)) and 636–641 nm light (for the 20× objective lens, Fig. 3(g)). As a result, the estimated wavelength-shift resolutions were approximately 0.047 nm (for the 4× objective lens in Fig. 3(f); see details in Table S3 in Section S8 in Appendix A) and about 0.033 nm (for the 20× objective lens in Fig. 3(h); see details in Table S4 in Section S8 in Appendix A), which are slightly larger than the calculated resolutions in the air environment (i.e., Figs. 3(b) and (d)) due to the larger fluctuation in the liquid environment. Next, we introduced a series of glycerol–water solutions (i.e., 0%, 3%, 6%, and 9%) to tune the refractive index of the liquid environment (see experimental details in Section S10 in Appendix A). As shown in Fig. 3(i), the centroid position shifts as the bulk refractive index changes between 0% and 9%. The noise of the data observed by the 20× objective lens (the red curve) is 0.0131 μm, which is slightly better than that observed by the 4× objective lens (i.e., 0.0405 μm, the blue curve). Since the data-acquisition time for each frame (i.e., 0.2 s·$frame^{-1}$) and the waiting period between adjacent frames (i.e., 15 s) are both faster than the bulk refractive index change speed, the bulk refractive index change curve can be reflected accurately. As a result, the measured bulk refractive index sensing resolutions are 3.29×10^{-4} refractive index units (RIU; for the 4× objective lens) and 9×10^{-3} RIU (for the 20× objective lens). Considering the sensor area of 0.002 mm^2, this chip holds promise for use in biosensing applications. More specifically, it can be expected to resolve approximately 500 exosomes under the observation of a 20× objective lens (see estimation details in Section S11 in Appendix A). A better sensing performance is achievable using a higher end light source and cameras with lower noise, which is currently under investigation. Next, we employ this on-chip imager to demonstrate the specific sensing of biomolecules (i.e., exosomes).

4.3. On-chip sensing of exosomal epidermal growth factor receptor for lung cancer diagnosis

Exosomal epidermal growth factor receptor (EGFR) has been shown in recent studies to be a promising biomarker for lung cancer diagnosis [41–45], as it is overexpressed in more than 50% of lung cancer cases. Here, we demonstrate the potential application of the rainbow trapping chip in cancer diagnosis using lung cancer as the disease model and exosomal EGFR as the biomarker (Fig. 4(a); see details in Section S12 in Appendix A). As shown in Fig. 4(b), a 2 × 2 graded grating array (a total of four sensor units, with the period changing from 400 to 490 nm) was fabricated on the same chip. Under the illumination of a narrow band of light at 650 nm, the dark bars on all four gratings were observed simultaneously in the liquid environment. A series of layers were introduced on top of the sensor surface to enable the selective sensing of exosomal EGFR (Fig. 4(c); see details of surface treatment in Section S12). During this process, the reflection image of the four sensor units was recorded by the far-field imager every 15 s to monitor the surface binding events. By extracting the centroid positions of the dark bars, the expression of exosomal EGFR is calculated by the following:

$$E = \frac{P_{\text{EGFR+exosome}} - P_{\text{PBS}}}{P_{\text{PBS}} - P_{\text{water}}} \quad (1)$$

where P_{water}, P_{PBS}, and $P_{\text{EGFR+exosome}}$ are the centroid positions for water, poly(butylene succinate) (PBS), and EGFR and exosomes, respectively. The difference between P_{water} and P_{PBS} was used as the normalization factor to minimize chip-to-chip variation. The EGFR expression in exosomes from A549 non-small cell lung cancer (NSCLC) cells was first measured (Fig. 4(d)). A549 cell-derived exosomes at a concentration of 2×10^{10} exosomes per milliliter (exosomes·mL^{-1}) were flowed through the biochip. Based on the centroid movement, the exosomal EGFR expression level was determined to be 0.3357, with a high signal-to-noise ratio of 10.39. With A549 cell-derived exosomes, the rainbow trapping chip achieved a resolution of 1.92×10^9 exosomes·mL^{-1}, suggesting that it may require as little as 1 μL of serum sample for the detection of exosomal EGFR, as the typical exosome concentration in serum is 5×10^{12} exosomes·mL^{-1}.

Next, the levels of exosomal EGFR in serum samples from three healthy controls and three NSCLC patients were measured (characteristics of the human subjects are provided in Table S6 in Section S13 in Appendix A). Exosomes were isolated from 80 μL of human serum samples, resuspended in 100 μL PBS, and flowed through the biochip at a concentration of 6×10^{10} exosomes·mL^{-1}. Representative real-time centroid movement curves of one healthy control and one NSCLC patient from one sensor unit are shown in Fig. 4(e) (also see all data in Section S14 in Appendix A). An obvious centroid shift was observed for the NSCLC patient sample, while little centroid shift was observed for the healthy control sample. With this 2 × 2 graded grating array, four measurements from four sensor units were performed simultaneously for each sample to improve the sensing accuracy. As shown in Fig. 4(f), good agreement (with coefficients of variation < 20%) among the results from the four sensor units were observed for all six human serum samples. The average expression of exosomal EGFR in sera from the NSCLC patients was 0.99 (indicated by the green line in Fig. 4(g)), which was about 8.25-fold higher than that in sera from the healthy controls (indicated by the orange line in Fig. 4(g)). Thus, the rainbow trapping chip successfully distinguished NSCLC patients from health controls using exosomal EGFR as the biomarker.

Furthermore, these rainbow trapping metasurface chips can be easily cleaned without damaging the nanostructures, and have shown excellent regenerability for repeated usages (see more details in Section S15 in Appendix A). These results demonstrate that the plasmonic rainbow trapping metasurface structure holds great potential for enabling ultra-sensitive and specific sensing of exosomal protein biomarkers for cancer diagnosis [46], especially using inexpensive optical systems that are conveniently assessable in daily life (e.g., Refs. [47,48]).

5. Conclusions

In conclusion, we have developed a plasmonic graded metasurface chip to trap "rainbow" plasmons in the visible to near-infrared

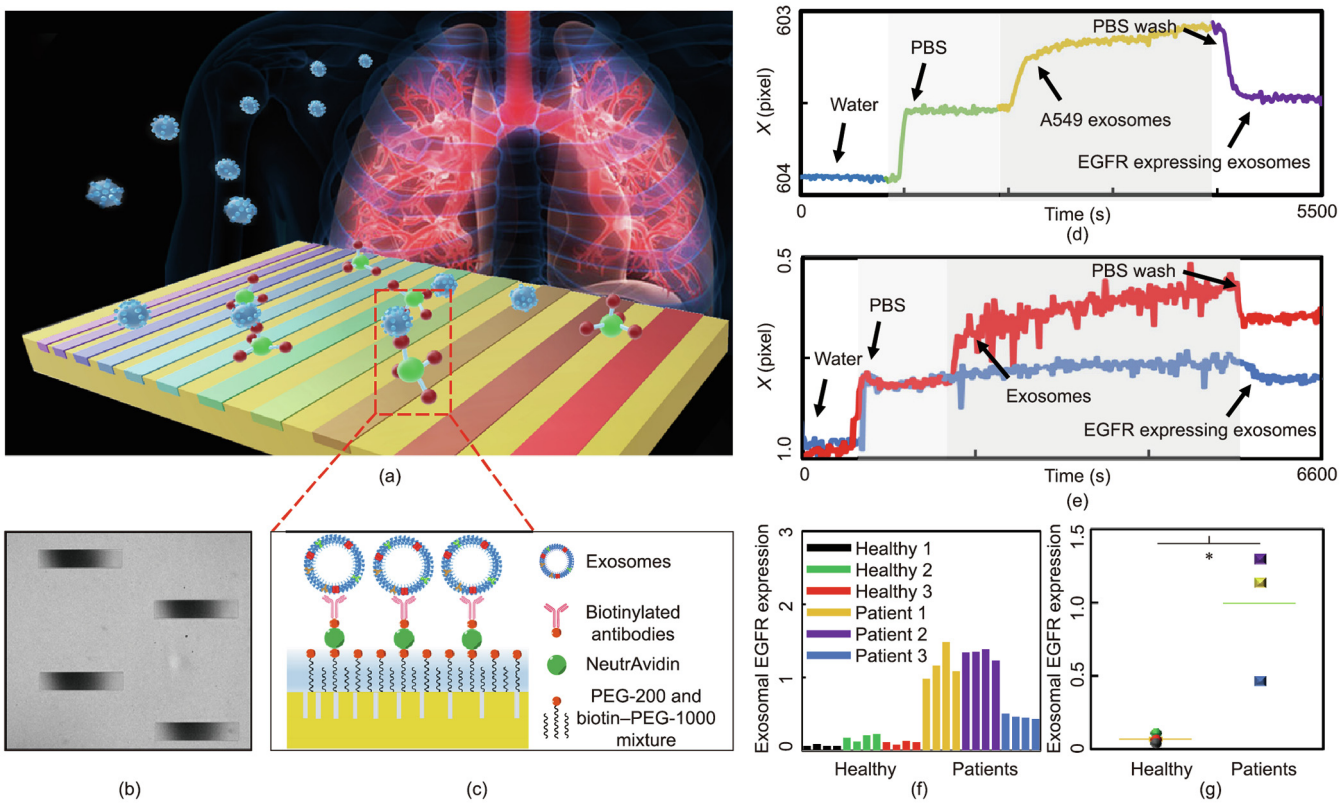

Fig. 4. Sensor arrays for lung cancer diagnosis. (a) Schematic diagram of the rainbow trapping metasurface used in lung cancer diagnosis. (b) SEM image of a sensor array with four identical graded metasurface structures. (c) Schematic diagram of the surface grating with captured EGFR and exosomes (PEG: polyethylene glycol). (d, e) Real-time response of the centroid displacement upon (d) A549 and (e) healthy control 1 (blue curve) and patient 1 (red curve) sample exosome adsorption on the sensor surface. (f) Exosomal EGFR expression of healthy controls and NSCLC patient samples measured by four sensor units on the chip. (g) Average exosomal EGFR expression of healthy controls and NSCLC patient samples. Orange and green bars indicate the means of three samples in each group. Significantly higher expression of exosomal EGFR was observed in the NSCLC patient samples than in those of the healthy controls ($n = 3$; $^*p < 0.05$).

domain. By extracting the numerical centroid of the trapped surface plasmon waves, a miniaturized imager-based platform was demonstrated for super-resolution displacement spectroscopic analysis and surface biosensing. Using a 4× optical microscope system, a displacement of the resonant position within 35 nm was resolved, corresponding to a spectral resolution of 0.032 nm in wavelength shift and a refractive index change of 5×10^{-4} RIU. Remarkably, the dimensions of this unique rainbow trapping imager chip are in an area range of 0.00192–0.01250 mm^2, enabling the characterization of spectroscopic information within tiny areas, which is impossible to do using conventional fiber-based spectrometers.

This low-setting imaging-based spectroscopic chip was used to detect A549-derived exosomes with a sensing resolution of 1.92×10^9 exosomes·mL^{-1}. Furthermore, we employed a 2×2 array of the rainbow chip to distinguish cancer patients from healthy control samples using exosomal EGFR expression, thereby successfully demonstrating the chip's application for cancer diagnosis, with great potential impact on point-of-care diagnostics. Although the accuracy of fabrication techniques sets a barrier for broader applications in a wide spectral range (from visible to telecommunication) [6–9], this limitation may be partially addressed by advanced fabrication techniques and photonic topological elements [11]. Moreover, by using scalable template stripping processes, it is possible to overcome the cost barrier and improve the surface smoothness of the graded gratings for improved coupling of SPP modes (e.g., Ref. [49]). Importantly, this imaging-based spectroscopic displacement strategy is fully amenable to machine learning algorithms (as is currently under investigation) and could result in intelligent spectroscopic chips on smart phones for personalized accurate biological or chemical sensing applications [50].

Acknowledgments

This work was partially supported by the National Science Foundation (ECCS-1807463 and PFI-1718177) and UB Blue Sky program. We appreciate Mr. Dylan Tua for helpful discussion on technical details. The authors also acknowledge funding support from National Cancer Institute (NCI) of the National Institutes of Health (NIH) (R21CA235305). Deidentified human serum samples and their clinical data for this study were provided by the Data Bank and BioRepository (DBBR), which is funded by NCI (P30CA16056) and is a Roswell Park Cancer Institute Cancer Center Support Grant shared resource. The content is solely the responsibility of the authors and does not necessarily represent the official views of NIH. The authors thank the support from National Science Foundation (CBET-1337860), which funds the nanoparticle tracking analysis system (NanoSight, LM10, Malvern Instruments, Ltd.).

Authors' contributions

Qiaoqiang Gan conceived the idea and supervised the project. Lyu Zhou, Nan Zhang, Chang Chieh Hsu, Matthew Singer, and Yizheng Li executed the experiments. Chang Chieh Hsu and Yun Wu prepared the biological samples. All authors contributed to the analysis of the experimental results and modeling. Lyu Zhou,

Nan Zhang, Matthew Singer, Josep Jornet, Yun Wu, and Qiaoqiang Gan wrote the manuscript. All authors reviewed the manuscript. Lyu Zhou and Nan Zhang are co-first authors and contributed equally.

Compliance with ethics guidelines

Lyu Zhou, Nan Zhang, Chang Chieh Hsu, Matthew Singer, Xie Zeng, Yizheng Li, Haomin Song, Josep Jornet, Yun Wu, and Qiaoqiang Gan declare that they have no conflict of interest or financial conflicts to disclose.

Appendix A. Supplementary data

Supplementary data to this article can be found online at https://doi.org/10.1016/j.eng.2022.03.018.

References

[1] Tsakmakidis KL, Hess O, Boyd RW, Zhang X. Ultraslow waves on the nanoscale. Science 2017;358(6361):eaan5196.
[2] Gao Z, Wu L, Gao F, Luo Y, Zhang B. Spoof plasmonics: from metamaterial concept to topological description. Adv Mater 2018;30(31):1706683.
[3] Tsakmakidis KL, Pickering TW, Hamm JM, Page AF, Hess O. Completely stopped and dispersionless light in plasmonic waveguides. Phys Rev Lett 2014;112 (16):167401.
[4] Baba T. Slow light in photonic crystals. Nat Photonics 2008;2(8):465–73.
[5] Tsakmakidis KL, Boardman AD, Hess O. 'Trapped rainbow' storage of light in metamaterials. Nature 2007;450(7168):397–401.
[6] Gan Q, Fu Z, Ding YJ, Bartoli FJ. Ultrawide-bandwidth slow-light system based on THz plasmonic graded metallic grating structures. Phys Rev Lett 2008;100 (25):256803.
[7] Gan Q, Ding YJ, Bartoli FJ. "Rainbow" trapping and releasing at telecommunication wavelengths. Phys Rev Lett 2009;102(5):056801.
[8] Gan Q, Gao Y, Wagner K, Vezenov D, Ding YJ, Bartoli FJ. Experimental verification of the rainbow trapping effect in adiabatic plasmonic gratings. Proc Natl Acad Sci USA 2011;108(13):5169–73.
[9] Gan Q, Bartoli FJ. Surface dispersion engineering of planar plasmonic chirped grating for complete visible rainbow trapping. Appl Phys Lett 2011;98 (25):251103.
[10] Leitis A, Tseng ML, John-Herpin A, Kivshar YS, Altug H. Wafer-scale functional metasurfaces for mid-infrared photonics and biosensing. Adv Mater 2021;33 (43):2102232.
[11] Tsakmakidis KL, Baskourelos K, Stefański T. Topological, nonreciprocal, and multiresonant slow light beyond the time-bandwidth limit. Appl Phys Lett 2021;119(19):190501.
[12] Tsakmakidis KL, Hess O. Extreme control of light in metamaterials: complete and loss-free stopping of light. Phys B 2021;407(20):4066–9.
[13] Li J, Yu P, Zhang S, Liu N. Electrically-controlled digital metasurface device for light projection displays. Nat Commun 2020;11(1):3574.
[14] Zhirihin DV, Kivshar YS. Topological photonics on a small scale. Small Sci 2021;1(12):2100065.
[15] Yang Z, Albrow-Owen T, Cai W, Hasan T. Miniaturization of optical spectrometers. Science 2021;371(6528):eabe0722.
[16] Yang Z, Albrow-Owen T, Cui H, Alexander-Webber J, Gu F, Wang X, et al. Single-nanowire spectrometers. Science 2019;365(6457):1017–20.
[17] Xu T, Wu YK, Luo X, Guo LJ. Plasmonic nanoresonators for high-resolution colour filtering and spectral imaging. Nat Commun 2010;1(1):59.
[18] Chen L, Wang GP, Gan Q, Bartoli FJ. Trapping of surface-plasmon polaritons in a graded Bragg structure: frequency-dependent spatially separated localization of the visible spectrum modes. Phys Rev B 2009;80(16):161106.
[19] Chen L, Wang GP, Gan Q, Bartoli FJ. Rainbow trapping and releasing by chirped plasmonic waveguides at visible frequencies. Appl Phys Lett 2010;97 (15):153115.
[20] Hu H, Ji D, Zeng X, Liu K, Gan Q. Rainbow trapping in hyperbolic metamaterial waveguide. Sci Rep 2013;3(1):1249.
[21] Jang MS, Atwater H. Plasmonic rainbow trapping structures for light localization and spectrum splitting. Phys Rev Lett 2011;107(20):207401.
[22] Ouyang L, Meyer-Zedler T, See KM, Chen WL, Lin FC, Akimov D, et al. Spatially resolving the enhancement effect in surface-enhanced coherent anti-Stokes Raman scattering by plasmonic Doppler gratings. ACS Nano 2021;15 (1):809–18.
[23] Lin FC, See KM, Ouyang L, Huang YX, Chen YJ, Popp J, et al. Designable spectrometer-free index sensing using plasmonic Doppler gratings. Anal Chem 2019;91(15):9382–7.
[24] See KM, Lin FC, Huang JS. Design and characterization of a plasmonic Doppler grating for azimuthal angle-resolved surface plasmon resonances. Nanoscale 2017;9(30):10811–9.
[25] Triggs GJ, Wang Y, Reardon CP, Fischer M, Evans GJO, Krauss TF. Chirped guided-mode resonance biosensor. Optica 2017;4(2):229–34.
[26] Tittl A, Leitis A, Liu M, Yesilkoy F, Choi DY, Neshev DN, et al. Imaging-based molecular barcoding with pixelated dielectric metasurfaces. Science 2018;360 (6393):1105–9.
[27] Yesilkoy F, Arvelo ER, Jahani Y, Liu M, Tittl A, Cevher V, et al. Ultrasensitive hyperspectral imaging and biodetection enabled by dielectric metasurfaces. Nat Photonics 2019;13(6):390–6.
[28] Leitis A, Tittl A, Liu M, Lee BH, Gu MB, Kivshar YS, et al. Angle-multiplexed all-dielectric metasurfaces for broadband molecular fingerprint retrieval. Sci Adv 2019;5(5):eaaw2871.
[29] Jahani Y, Arvelo ER, Yesilkoy F, Koshelev K, Cianciaruso C, De Palma M, et al. Imaging-based spectrometer-less optofluidic biosensors based on dielectric metasurfaces for detecting extracellular vesicles. Nat Commun 2021;12 (1):3246.
[30] Schuller JA, Barnard ES, Cai W, Jun YC, White JS, Brongersma ML. Plasmonics for extreme light concentration and manipulation. Nat Mater 2010;9 (3):193–204.
[31] Koenderink AF, Alù A, Polman A. Nanophotonics: shrinking light-based technology. Science 2015;348(6234):516–21.
[32] Oh SH, Altug H. Performance metrics and enabling technologies for nanoplasmonic biosensors. Nat Commun 2018;9(1):5263.
[33] Gould TJ, Hess ST, Bewersdorf J. Optical nanoscopy: from acquisition to analysis. Annu Rev Biomed Eng 2012;14(1):231–54.
[34] Mejía-Salazar JR, Oliveira Jr ON. Plasmonic biosensing. Chem Rev 2018;118 (20):10617–25.
[35] Gao Y, Xin Z, Zeng B, Gan Q, Cheng X, Bartoli FJ. Plasmonic interferometric sensor arrays for high-performance label-free biomolecular detection. Lab Chip 2013;13(24):4755–64.
[36] Gao Y, Gan Q, Xin Z, Cheng X, Bartoli FJ. Plasmonic Mach–Zehnder interferometer for ultrasensitive on-chip biosensing. ACS Nano 2011;5 (12):9836–44.
[37] Small A, Stahlheber S. Fluorophore localization algorithms for super-resolution microscopy. Nat Methods 2014;11(3):267–79.
[38] Pertsinidis A, Zhang Y, Chu S. Subnanometre single-molecule localization, registration and distance measurements. Nature 2010;466(7306):647–51.
[39] Qu X, Wu D, Mets L, Scherer NF. Nanometer-localized multiple single-molecule fluorescence microscopy. Proc Natl Acad Sci USA 2004;101 (31):11298–303.
[40] Ocean Optics, Inc. Jaz installation and operation manual. Dunedin: Ocean Optics, Inc.; 2010.
[41] Vlassov AV, Magdaleno S, Setterquist R, Conrad R. Exosomes: current knowledge of their composition, biological functions, and diagnostic and therapeutic potentials. Biochim Biophys Acta 2012;1820(7):940–8.
[42] Yamashita T, Kamada H, Kanasaki S, Maeda Y, Nagano K, Abe Y, et al. Epidermal growth factor receptor localized to exosome membranes as a possible biomarker for lung cancer diagnosis. Pharmazie 2013;68(12):969–73.
[43] Jakobsen KR, Paulsen BS, Bæk R, Varming K, Sorensen BS, Jørgensen MM. Exosomal proteins as potential diagnostic markers in advanced non-small cell lung carcinoma. J Extracell Vesicles 2015;4(1):26659.
[44] Sandfeld-Paulsen B, Aggerholm-Pedersen N, Baek R, Jakobsen KR, Meldgaard P, Folkersen BH, et al. Exosomal proteins as prognostic biomarkers in non-small cell lung cancer. Mol Oncol 2016;10(10):1595–602.
[45] Clark DJ, Fondrie WE, Yang A, Mao L. Triple SILAC quantitative proteomic analysis reveals differential abundance of cell signaling proteins between normal and lung cancer-derived exosomes. J Proteomics 2016;133:161–9.
[46] Liang Y, Lehrich BM, Zheng S, Lu M. Emerging methods in biomarker identification for extracellular vesicle-based liquid biopsy. J Extracell Vesicles 2021;10(7):e12090.
[47] Yanik AA, Cetin AE, Huang M, Artar A, Mousavi SH, Khanikaev A, et al. Seeing protein monolayers with naked eye through plasmonic Fano resonances. Proc Natl Acad Sci USA 2011;108(29):11784–9.
[48] Zhu H, Isikman SO, Mudanyali O, Greenbaum A, Ozcan A. Optical imaging techniques for point-of-care diagnostics. Lab Chip 2013;13(1):51–67.
[49] Lindquist NC, Johnson TW, Norris DJ, Oh SH. Monolithic integration of continuously tunable plasmonic nanostructures. Nano Lett 2011;11 (9):3526–30.
[50] Ballard Z, Brown C, Madni AM, Ozcan A. Machine learning and computation-enabled intelligent sensor design. Nat Mach Intell 2021;3(7):556–65.